

Enhanced pH-Universal Hydrogen Evolution Reactions on the Ru/*a*-Ni-MoO₃ Electrocatalysts

Lingyi Peng, Ding Zhang, Zhipeng Ma, Dewei Chu, Claudio Cazorla, Rose Amal, and Zhaojun Han*

Green hydrogen production through the electrocatalytic hydrogen evolution reaction (HER) is a promising solution for transition from fossil fuels to renewable energy. To enable the use of a variety of electrolytes with different pH values, HER catalysts with pH universality are highly desirable but their performance remains mediocre. Herein, a pH-universal HER catalyst composed of ruthenium nanoparticles decorated on amorphous Ni-doped MoO₃ (*a*-Ni-MoO₃) nanowire support is reported, that is, Ru/*a*-Ni-MoO₃, which achieves enhanced performance as compared to the commercial Ru/C catalyst. Electron transfer from Ru to *a*-Ni-MoO₃ is identified by spectroscopic techniques, which results in a modified electronic structure of the Ru active sites with a reduced electron density of 4*d* states near the Fermi level. Density functional theory calculations further reveal that the modulated electronic structure weakens the interactions between the Ru active sites and the reaction intermediates, which facilitates the HER reaction steps including H intermediate desorption and water dissociation. Experimental and theoretical findings provide insight into enhancing pH-universal HER performance through modulation of electrocatalyst electronic structure.

1. Introduction

To tackle global warming and reduce carbon emission, it is of great importance to shift our energy source from fossil fuels to renewable energy. Electrocatalytic hydrogen evolution reaction (HER), which transforms energy into the chemical energy stored in green hydrogen (H₂), provides an efficient and sustainable way for better energy utilization.^[1] In practice, HER can be performed using different water feeds including purified water-based media (e.g., acidic, alkaline, and neutral media) and low-grade waters such as unbuffered seawater and wastewater.^[2–9] The vastly different pH values among these scenarios (typically from 0 to 14) and potential local pH changes during HER call for the need of developing pH-universal catalysts.^[10] Unfortunately, many HER catalysts are restricted by their intrinsic properties and can only function in a narrow range of

pH values, owing to several reasons: first, pH-universal HER requires catalysts to have proper adsorption sites to different reaction intermediates, which often makes single-component catalysts incompetent as the HER mechanisms vary in different media^[11]; second, the stability of catalysts is dependent on the pH value of the electrolyte, for example, Earth-abundant transition metals (e.g., Ni, Co) can have decent performance in alkaline media but exhibit limited stability in acidic media.^[12] By alloying these metal elements with nonmetallic elements (e.g., C, P, S, etc.), the performance of the resultant compounds in acidic media can be enhanced, but they are often prone to surface reconstruction and degradation in alkaline media.^[13–15]

Ruthenium (Ru) recently emerged as a HER catalyst with good potential in pH-universal HER due to its merits in different scenarios. In acidic media where dissolution is a common challenge for metal-based catalysts, Ru has better stability than many non-precious metal-based catalysts due to its large thermodynamic window.^[16] In nonacidic media where the bottleneck of HER is often the sluggish water dissociation process, the high affinity of Ru to hydroxyl intermediate (OH*) can help enhance the reaction rate.^[17] In addition, the unit price of Ru is only about a half of that of the HER benchmark catalyst Pt, making it a low-cost option to substitute Pt in large scale applications.^[18] Nevertheless, Ru is intrinsically less active than Pt in HER due to its strong binding energy to H intermediate (H*).

L. Peng, D. Zhang, Z. Ma, R. Amal, Z. Han
School of Chemical Engineering
The University of New South Wales
Sydney, NSW 2052, Australia
E-mail: zhaojun.han@unsw.edu.au

D. Chu
School of Materials Science and Engineering
The University of New South Wales
Sydney, NSW 2052, Australia

C. Cazorla
Department of Physics
Polytechnic University of Catalonia (UPC)
08034 Barcelona, Spain

Z. Han
CSIRO Manufacturing
Lindfield, NSW 2070, Australia

 The ORCID identification number(s) for the author(s) of this article can be found under <https://doi.org/10.1002/sstr.202300194>.

© 2023 The Authors. Small Structures published by Wiley-VCH GmbH. This is an open access article under the terms of the Creative Commons Attribution License, which permits use, distribution and reproduction in any medium, provided the original work is properly cited.

DOI: 10.1002/sstr.202300194

As depicted by density functional theory (DFT) calculations, the calculated H^* adsorption Gibbs free energy (ΔG_{H^*}) is often used as a descriptor for HER catalytic activity (the so-called volcano plot).^[19] Pt exhibits close to thermal-neutral ΔG_{H^*} (≈ 0), facilitating both the H^* adsorption and desorption processes which leads to optimal activity. In contrast, Ru exhibits negative ΔG_{H^*} values, indicating its strong binding to H^* .^[20,21] This strong binding would impede the recombination and desorption of H_2 , resulting in a high energy barrier and consequently inferior HER kinetics. In light of this, modulating the electronic structure to achieve an optimal binding to H^* represents a feasible approach to improve the pH-universal HER performance of Ru-based catalysts.

Herein, we report a facile method to fabricate a catalyst composed of Ru nanoparticles decorated on amorphous Ni-doped MoO_3 (α -Ni- MoO_3) nanowire support, i.e., Ru/ α -Ni- MoO_3 , which exhibits enhanced HER performance over a wide range of pH values as compared to the Ru/C counterpart. Through a combination of experimental investigations, it is demonstrated that Ru donates electrons to the α -Ni- MoO_3 support, resulting in a modulated electronic structure of the Ru active sites with a decreased electron density of $4d$ states near the Fermi level. Further theoretical calculations reveal that the modulated electronic structure weakens the interaction between the Ru active

sites and the reaction intermediates, which alleviates the strong adsorption of Ru to H^* and facilitates the H^* desorption. The modulated electronic structure also helps achieve an optimized water dissociation step in non-acidic media with a reduced kinetic energy barrier. Our work demonstrates the importance of electronic structure modulation in catalysts to achieve favorable HER thermodynamics and kinetics, shedding light on the design of more effective pH-universal catalysts.

2. Results and Discussion

2.1. Fabrication, Structure, and Electronic State of Ru/ α -Ni- MoO_3

The fabrication process of Ru/ α -Ni- MoO_3 on activated carbon cloth (ACC) substrate is illustrated in **Figure 1a**. Briefly, ACC with good hydrophilicity was used as a substrate for the hydrothermal growth of $NiMoO_4$.^[22] The as-obtained $NiMoO_4$ was then reduced in the H_2/Ar atmosphere at $400^\circ C$ (denoted as $NiMoO_4-R$). Subsequently, $NiMoO_4-R$ was immersed in 1 mg mL^{-1} $RuCl_3$ solution to obtain Ru/ α -Ni- MoO_3 through the spontaneous redox reaction between Ru^{3+} and the metallic Ni in $NiMoO_4-R$.^[21] An immersion time of 22 h was applied to

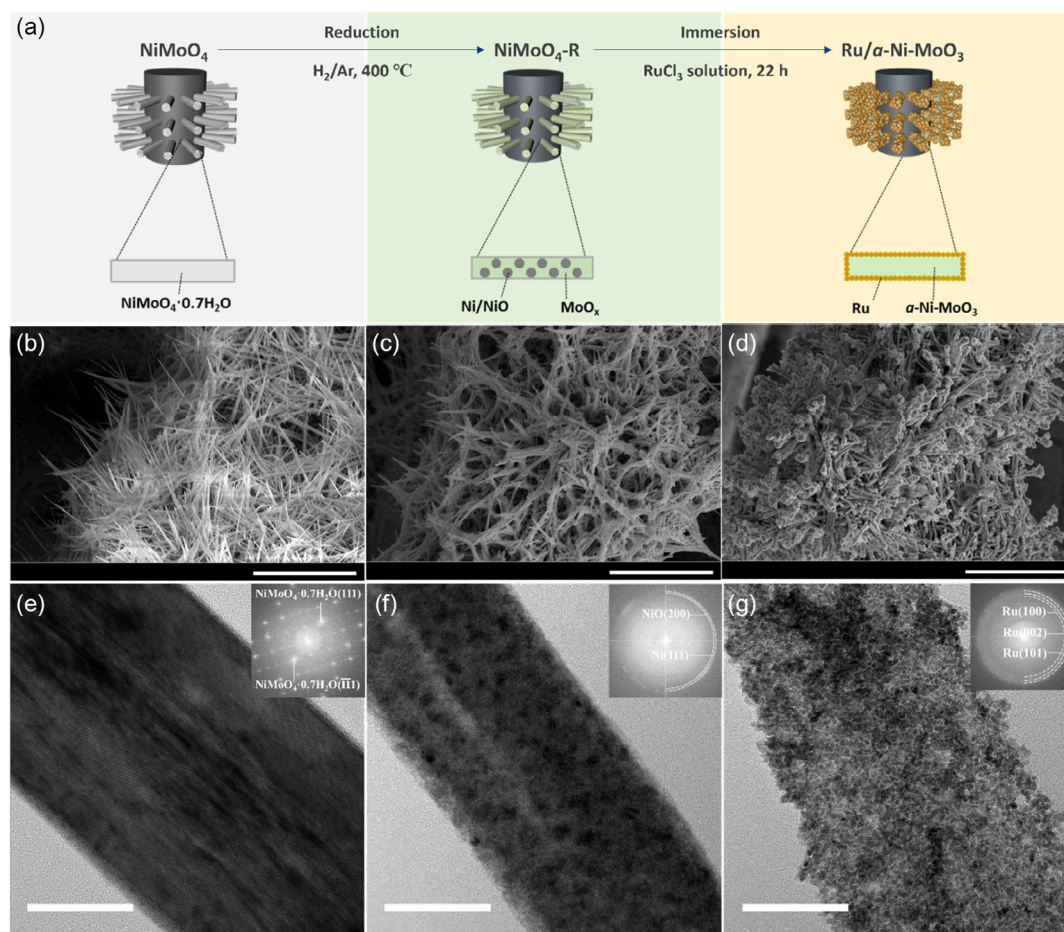


Figure 1. a) Schematic illustration of the fabrication process of Ru/ α -Ni- MoO_3 . b–d) SEM images of $NiMoO_4$, $NiMoO_4-R$, and Ru/ α -Ni- MoO_3 ; scale bars: $10\ \mu\text{m}$. e–g) TEM images of $NiMoO_4$, $NiMoO_4-R$, and Ru/ α -Ni- MoO_3 ; scale bars: $50\ \text{nm}$; insets show the corresponding FFT images.

guarantee sufficient reaction and stable catalytic performance (Figure S1, Supporting Information). After 22 h immersion, a Ru mass loading of 0.35 mg cm^{-2} was determined by inductively coupled plasma–mass spectrometry (ICP-MS) (Table S1, Supporting Information). Figure 1b–g shows the morphological evolution revealed by scanning electron microscopy (SEM) and transmission electron microscopy (TEM). In Figure 1b, the SEM image of NiMoO_4 showed nanowires grown on the ACC substrate. The TEM image and corresponding fast-Fourier transform (FFT) image (Figure 1e) indicated that the nanowires were single-crystalline NiMoO_4 hydrate (PDF 04-017-0338), which was consistent with the X-ray diffraction (XRD) pattern (Figure S2a, Supporting Information) and the selected-area electron diffraction (SAED) pattern (Figure S3a, Supporting Information). For $\text{NiMoO}_4\text{-R}$, the nanowire morphology was maintained (Figure 1c,f), while the phase composition changed to crystalline metallic Ni (PDF 00-004-0850) and NiO (PDF 01-073-1519) as a result of thermal reduction (Figures S2b and S3b, Supporting Information). The embedded nanoparticles as seen in the TEM image were primarily aggregated Ni (Figure S4, Supporting Information). No crystalline Mo phases could be identified, indicating that Mo species were likely to be amorphous.^[23]

For the final product $\text{Ru}/a\text{-Ni-MoO}_3$ (Figure 1d,g), nanoparticles decorated on the nanowires could be seen from both SEM and TEM images. The average size of the nanoparticles was $\approx 2.8 \text{ nm}$ (Figure S5, Supporting Information). Crevices and possible mesopores ($\approx 3\text{--}5 \text{ nm}$) could be observed among the nanoparticles, ensuring efficient mass transfer (Figure S6, Supporting Information).^[24] The crystalline features in the FFT image and SAED pattern could be solely assigned to metallic hexagonal-close-packed (hcp) Ru (PDF 04-011-9035) (Figure S3c, Supporting Information), indicating that Ru was the predominant crystalline phase while other species were likely of amorphous nature. In comparison with $\text{NiMoO}_4\text{-R}$, the disappearance of crystalline Ni phase in $\text{Ru}/a\text{-Ni-MoO}_3$ suggested that Ni acted as a sacrificial agent in the immersion step, while the absence of crystalline NiO phase was due to its dissolution in the acidic RuCl_3 solution ($\text{pH} \approx 3$). Indeed, the quantitative elemental analysis by inductively coupled plasma–optical emission spectrometry (ICP-OES) showed gradually decreased Ru concentration and increased Ni concentration along with the immersion time (Figure S7, Supporting Information). The concentration of Mo species in the solution remained at a low level throughout the immersion process, indicating that they were not soluble. Based on these microscopic and spectroscopic results, the formation reaction of Ru on $a\text{-Ni-MoO}_3$ was given as $3\text{Ni} + 2\text{Ru}^{3+} \rightarrow 3\text{Ni}^{2+} + 2\text{Ru}$.

Next, a combination of physicochemical characterizations was carried out to reveal its structure and electronic state in detail. The scanning transmission electron microscopy–energy-dispersive X-ray spectroscopy (STEM-EDS) mapping showed the distributions of O, Ni, Mo, and Ru elements (Figure 2a). Quantitative analysis revealed metal atomic ratios of Ru:Mo:Ni = 82:16:2 with a clear dominance of Ru (Figure S8, Supporting Information). It could be seen that there were some areas with weaker signals of Ru than other elements, indicating that Ru nanoparticles were decorated on the $a\text{-Ni-MoO}_3$

substrate instead of a complete coverage. This could also explain the different ratios of Ru:Mo:Ni = 62:22:15 from the ICP-MS measurement, which revealed the elemental contents in the whole electrode (Table S1, Supporting Information). The partial coverage resulted from the termination of Ru deposition after depleting the finite amount of metallic Ni in $\text{NiMoO}_4\text{-R}$. In addition, the surfactant-free environment could also contribute to the partial coverage because nanoparticles would favor aggregated growth due to their high surface energy.^[25] The high-resolution TEM (HRTEM) image indicated coexisting crystalline Ru nanoparticles and amorphous Ni-MoO₃ regions with clear interfaces between them, where the characteristic lattice spacing of 0.215 nm corresponded to the Ru (002) facets (Figure 2b).

Raman spectroscopy was also performed to give more information on the amorphous species. As shown in Figure 2c, the reference crystalline MoO_3 spectrum had three major Raman bands with peak positions at 995, 665, and 818 cm^{-1} , which could be assigned to the stretching modes of terminal oxygen (Mo=O), triply connected bridge oxygen (Mo₃-O), and doubly connected bridge oxygen (Mo₂-O), respectively.^[26] In contrast, the spectrum of $\text{Ru}/a\text{-Ni-MoO}_3$ only showed one broad peak positioned at $\approx 863 \text{ cm}^{-1}$, ascribed to the predominant Mo₂-O bonding structure. The shift and broadening of Raman peak were a result of the amorphous nature.^[26] Besides, no Raman bands corresponding to bulk NiO could be identified, suggesting that the Ni in $\text{Ru}/a\text{-Ni-MoO}_3$ was dopant rather than aggregate.^[27] In comparison with the bulk NiO phase in $\text{NiMoO}_4\text{-R}$ which was prone to dissolution during the immersion step, the Ni dopant confined in the $a\text{-Ni-MoO}_3$ lattice could be more corrosion resistant and thus was retained after immersion.^[28] It is reasonable to correlate the Ni dopant with the amorphousness of Ni-MoO₃, as doping is a common cause for amorphization.^[29] Collectively, these characterizations proved that the structure of $\text{Ru}/a\text{-Ni-MoO}_3$ was metallic hcp Ru anchored on the amorphous Ni-MoO₃ substrate.

Next, X-ray photoelectron spectroscopy (XPS) characterization was performed to give information on the surface chemical states of $\text{Ru}/a\text{-Ni-MoO}_3$. Figure 2d shows the Ru(IV) $3p_{3/2}$ and satellite peaks of Ru/C and $\text{Ru}/a\text{-Ni-MoO}_3$.^[30] Notably, the Ru $3p_{3/2}$ peak position of $\text{Ru}/a\text{-Ni-MoO}_3$ exhibited a shift of 0.44 eV in binding energy higher than that of Ru/C, suggesting that Ru in $\text{Ru}/a\text{-Ni-MoO}_3$ had a higher oxidation state as compared to that in Ru/C (the detailed peak positions and percentages are given in Table S2, Supporting Information). This finding was further corroborated by the analysis of Ru $3d$ spectra (Figure S9, Supporting Information), which were deconvoluted into Ru(IV) $3d_{5/2}$ and Ru(IV) $3d_{3/2}$ peaks, satellite peaks, and an overlapping carbon peak.^[30] Again, the Ru $3d$ peak positions of $\text{Ru}/a\text{-Ni-MoO}_3$ showed a shift to higher binding energy by 0.44 eV as compared to those of Ru/C. It was worth noting that while the surface of Ru nanoparticles exhibited an oxidized state of Ru(IV), possibly due to the oxidation when exposed to air during sample transfer,^[31] the bulk was still metallic Ru as suggested by the above SAED and HRTEM results.

The Mo $3d$ spectrum of $\text{Ru}/a\text{-Ni-MoO}_3$ in Figure 2e revealed that Mo was in the oxidized state with a mixture of Mo(IV), Mo(V), and Mo(VI) (the detailed peak positions and percentages are given in Table S3, Supporting Information), with Mo(VI) as

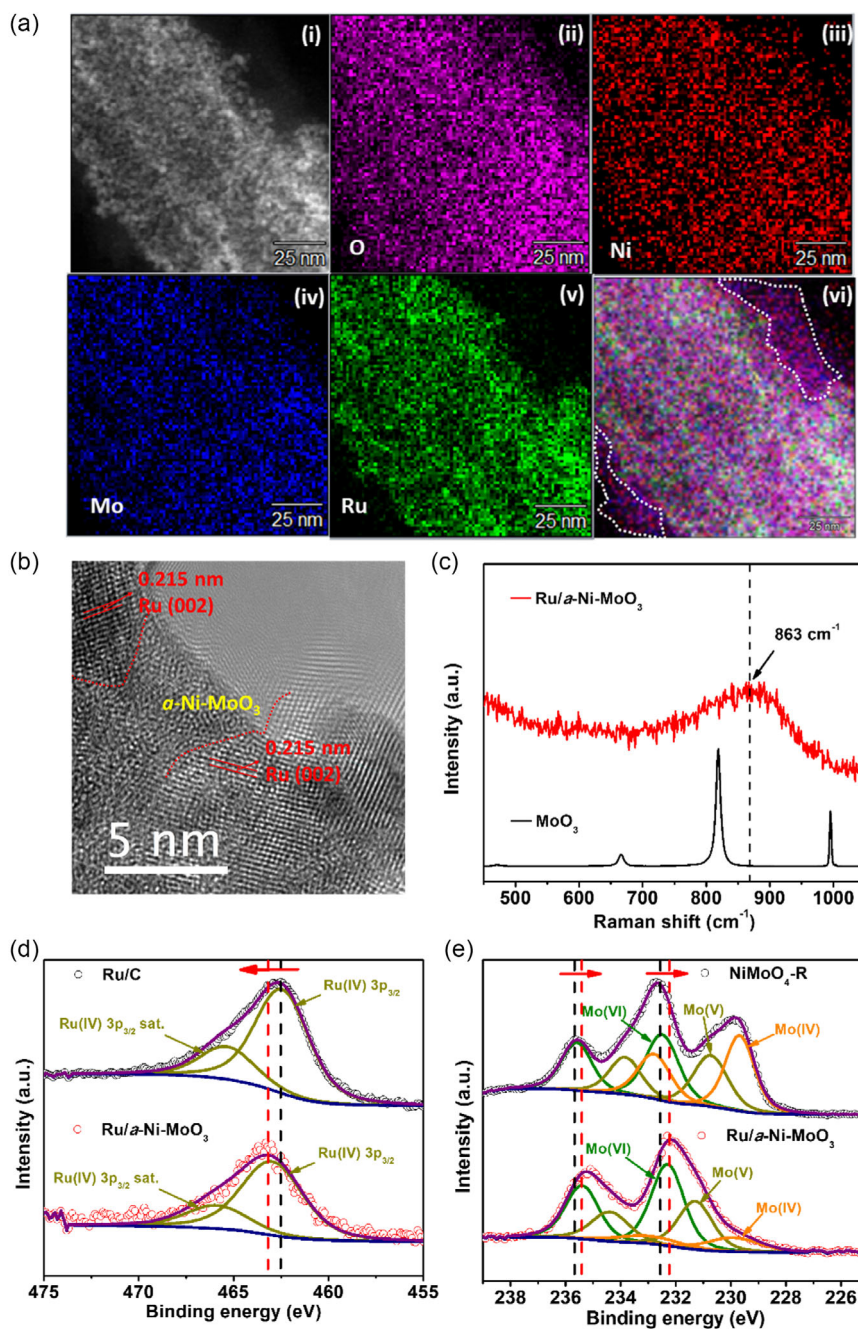


Figure 2. a) STEM (i) and the corresponding O (ii), Ni (iii), Mo (iv), Ru (v), and overlay elemental mapping (vi) images. b) HRTEM image of Ru/a-Ni-MoO₃. c) Raman spectra of Ru/a-Ni-MoO₃ and crystalline MoO₃ reference. d) High-resolution XPS Ru 3p_{3/2} spectra of Ru/C and Ru/a-Ni-MoO₃. e) High-resolution XPS Mo 3d spectra of NiMoO₄-R and Ru/a-Ni-MoO₃.

the dominant valence state (52.81%).^[32] In comparison, the Mo 3d spectrum of NiMoO₄-R had a lower concentration of Mo(VI) (35.38%). More importantly, the Mo(VI) peak positions in Ru/a-Ni-MoO₃ showed a shift to lower binding energy by 0.19 eV as compared to those in NiMoO₄-R, indicating the electron enrichment of Mo atoms in Ru/a-Ni-MoO₃. A similar phenomenon was also observed in the Ni 2p spectra. As shown in Figure S10, Supporting Information, the Ni 2p_{3/2} spectra of

NiMoO₄-R could be deconvoluted into Ni(0) and Ni(II) components (the detailed peak positions and percentages are given in Table S3, Supporting Information).^[33] In contrast, only Ni(II) was present in the spectra of Ru/a-Ni-MoO₃, with the peak position shifted to a lower binding energy by 0.46 eV. These results demonstrated the electronic interaction between Ru and the a-Ni-MoO₃ substrate, that is, electron transfer from Ru to the a-Ni-MoO₃.

Furthermore, ultraviolet photoelectron spectroscopy (UPS) was performed to probe the valence band structure. When small metal nanoparticles are deposited on oxides, they can exhibit reduced electron density of d states near the Fermi level, as a result of the electronic interaction between the metal and the oxide support.^[34] Indeed, as shown in Figure S11, Supporting Information, the UPS spectrum of Ru/*a*-Ni-MoO₃ exhibited a decrease in the electron density of Ru 4d states near the Fermi level as compared to that of Ru/C. This confirmed the charge transfer in Ru/*a*-Ni-MoO₃ and its modulation on the electronic structure of Ru.

2.2. pH-Universal HER Performance

To evaluate the electrocatalytic HER performance of Ru/*a*-Ni-MoO₃, electrolytes at different pH values were used, including pH = 0 (0.5 M H₂SO₄ as acidic media), pH = 7 (1 M phosphate buffer solution (PBS) as neutral media), and pH = 14 (1 M KOH as alkaline media). A typical

three-electrode configuration was employed, with the as-prepared Ru/*a*-Ni-MoO₃ on ACC electrode as the working electrode and a graphite rod as the counter electrode. For the reference electrode, a saturated calomel electrode (SCE) was used in acidic and neutral media, while HgO/Hg electrode was used in alkaline media. For comparison, Ru/C and Pt/C catalysts drop cast on ACC were used as control working electrodes at a similar noble metal loading (0.35 mg cm⁻²).

The HER performance in acidic media is presented in Figure 3a–c. As shown in the polarization curves (Figure 3a), the overpotentials required to deliver 10 mA cm⁻² (η_{10}) for Ru/C, Ru/*a*-Ni-MoO₃, and Pt/C were 42, 31, and 19 mV, respectively. At a larger current density, the disparity between Ru/C and Ru/*a*-Ni-MoO₃ became larger, with Ru/*a*-Ni-MoO₃ being able to maintain an activity closer to that of Pt/C. Specifically, the overpotentials to achieve 100 mA cm⁻² (η_{100}) for Ru/C, Ru/*a*-Ni-MoO₃, and Pt/C were 105, 61, and 32 mV, respectively. To better reflect the intrinsic activity, electrochemical surface area (ECSA)-normalized polarization curves were also plotted

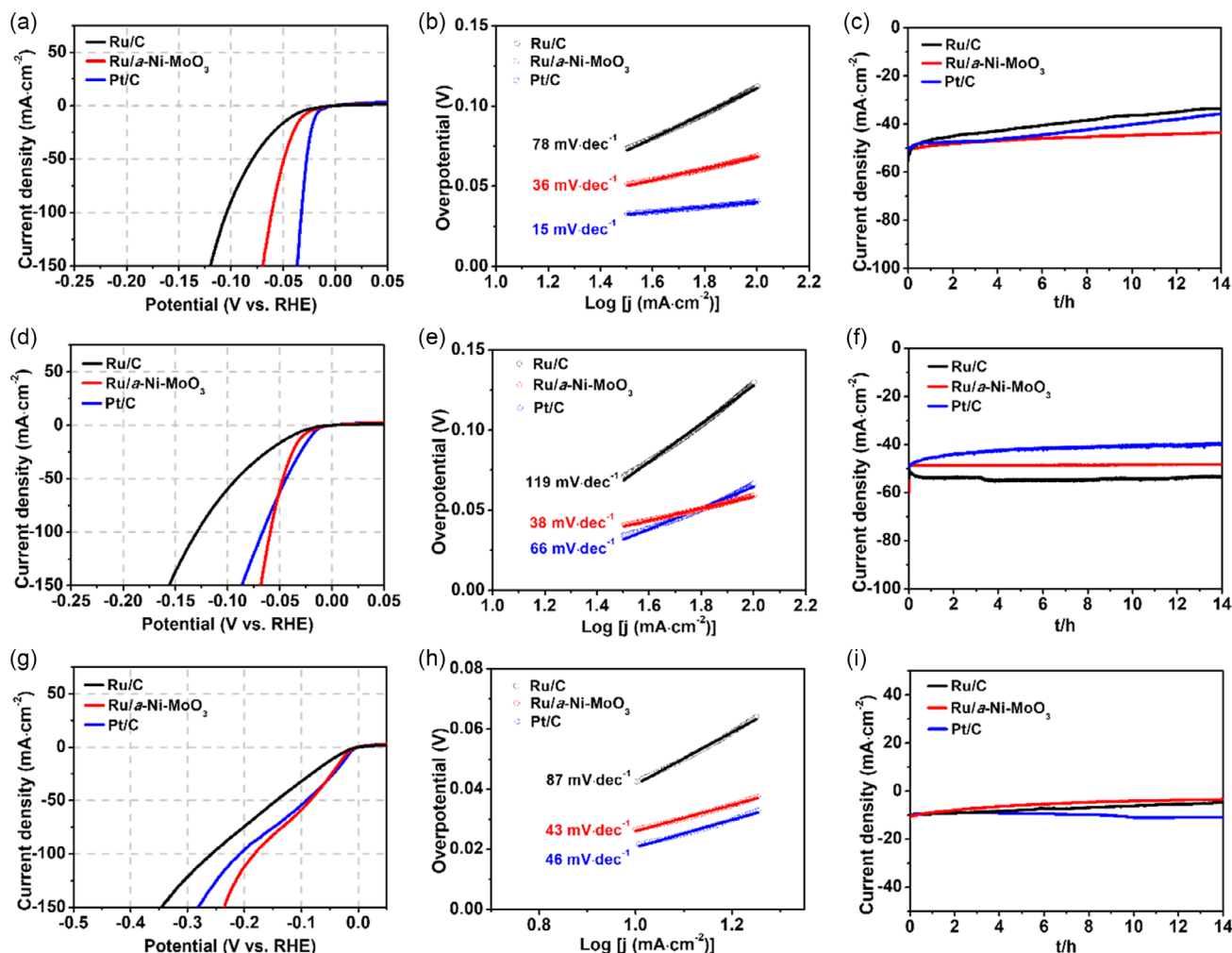


Figure 3. a) Polarization curves at a scan rate of 5 mV s⁻¹, b) Tafel plots, c) CA stability curves of Ru/C, Ru/*a*-Ni-MoO₃, and Pt/C in 0.5 M H₂SO₄ acidic media. d) Polarization curves at a scan rate of 5 mV s⁻¹, e) Tafel plots, and f) CA stability curves of Ru/C, Ru/*a*-Ni-MoO₃, and Pt/C in 1 M KOH alkaline media. g) Polarization curves at a scan rate of 5 mV s⁻¹, h) Tafel plots, and i) CA stability curves of Ru/C, Ru/*a*-Ni-MoO₃, and Pt/C in 1 M PBS neutral media.

(Figure S12 and S13, Supporting Information), which presented a similar trend and confirmed that Ru/*a*-Ni-MoO₃ was inherently more active than Ru/C.

To give more information on the HER kinetics and mechanism, Tafel plot analysis was further conducted. It is widely accepted that HER involves two steps. In acidic media, the first step (i.e., Volmer step) is the formation of H* from proton; and the second step is the formation from H* to H₂ molecule with two possible pathways, that is, the Heyrovsky step which is the electrochemical recombination between H* and another proton or the Tafel step which is the chemical recombination between two H*. The theoretical Tafel slope values are 118, 42, and 29 mV dec⁻¹ when the rate-determining step (RDS) is the Volmer, Heyrovsky, and Tafel steps, respectively.^[35] The Tafel slope of Ru/*a*-Ni-MoO₃ was 36 mV dec⁻¹ (Figure 3b), indicating a Volmer–Heyrovsky HER mechanism, with the Heyrovsky step as the RDS. Among the three catalysts, the Tafel slopes followed the order of Ru/C > Ru/*a*-Ni-MoO₃ > Pt/C, agreeing well with the above activity trend. Ru/*a*-Ni-MoO₃ also exhibited good stability, with current density retention of 86% after 14 h of chronoamperometry (CA) stability test, as compared to 70% and 61% for Pt/C and Ru/C respectively (Figure 3c, Table S4, Supporting Information). In addition, electrochemical impedance spectroscopy (EIS) was employed to give more information on the solid–electrolyte interfacial properties and HER kinetics (Figure S14 and S15, Supporting Information). The EIS spectra of Ru/*a*-Ni-MoO₃ showed a double-circle feature, with the one at high frequencies associated with the porosity of the electrode and the one at low frequencies ascribed to the charge transfer process in HER.^[36] The equivalent circuit parameters obtained from fitting (Table S5, Supporting Information) showed that the charge transfer resistance (*R*_{ct}) of Ru/*a*-Ni-MoO₃ (0.64 Ω) was much smaller than that of Ru/C (2.75 Ω), corresponding to a faster charge transfer kinetics. These results confirmed the enhanced HER performance of Ru/*a*-Ni-MoO₃ over Ru/C in acidic media.

The HER performance in alkaline media is shown in Figures 3d–f. As presented in the polarization curves, the η_{10} for Ru/C, Ru/*a*-Ni-MoO₃, and Pt/C were 39, 28, and 20 mV, respectively. At larger current densities, the performance of Ru/*a*-Ni-MoO₃ began to surpass that of Pt/C. For example, the η_{100} for Ru/C, Ru/*a*-Ni-MoO₃, and Pt/C were 130, 59, and 67 mV, respectively. The activity trend was also confirmed in the ECSA-normalized polarization curves (Figure S16 and S17, Supporting Information). It is noted that the Ru-based catalysts, especially Ru/*a*-Ni-MoO₃, presented comparable HER activities in alkaline media to those in acidic media, while the performance of Pt/C in alkaline media was inferior to that in acidic media. This could be attributed to the unique affinity to OH* of Ru facilitating alkaline HER, in accordance with previous studies.^[17,37] In the Tafel plots (Figure 3e), both Ru/C and Pt/C presented relatively large Tafel slopes (119 and 66 mV dec⁻¹ respectively), implying the Volmer step as the RDS. Indeed, due to the sluggish water dissociation process to provide H*, the Volmer step often becomes the RDS in alkaline media.^[11] In contrast, Ru/*a*-Ni-MoO₃ had a low Tafel slope of 38 mV dec⁻¹, suggesting that HER was not restricted by the water dissociation process and therefore the Heyrovsky step became the RDS. Besides high activity and fast kinetics, Ru/*a*-Ni-MoO₃ also exhibited excellent stability in alkaline

media, with negligible performance degradation after 14 h of stability test (Figure 3f, Table S4, Supporting Information). In contrast, the current density of Pt/C decreased by 20% after the same duration. Moreover, the EIS spectra and equivalent circuit fitting of Ru/*a*-Ni-MoO₃ (Figures S18 and S19, Table S5, Supporting Information) revealed a *R*_{ct} (0.19 Ω) smaller than that of Ru/C (1.3 Ω) and Pt/C (0.89 Ω), proving its fast charge transfer kinetics. These results collectively showed that Ru/*a*-Ni-MoO₃ had superior HER performance in alkaline media.

HER in neutral media is an emerging research field as it can benefit the production of green H₂ in a mild environment, for example, coupling water electrolysis with photovoltaics in the solar-to-hydrogen devices.^[38] The polarization curves in 1 M PBS (Figure 3g) indicated that η_{10} for Ru/C, Ru/*a*-Ni-MoO₃, and Pt/C were 42, 27, and 22 mV, respectively. At larger current densities, Ru/*a*-Ni-MoO₃ started to exhibit smaller overpotentials than Pt/C. For example, η_{100} for Ru/C, Ru/*a*-Ni-MoO₃, and Pt/C were 258, 182, and 208 mV, respectively. Again, the ECSA-normalized polarization curves showed a similar activity trend (Figure S20 and S21, Supporting Information). The mechanism of HER in neutral media is more complicated, which is generally accepted to resemble that in acidic media at low overpotentials, while being analogous to that in alkaline media at high overpotentials due to the depletion of protons.^[39] Indeed, while the Tafel slopes of Ru/*a*-Ni-MoO₃ were consistently much lower than those of Ru/C and in accordance with the above activity trend, dependence on overpotentials was observed when comparing with those of Pt/C: at low overpotentials, Ru/*a*-Ni-MoO₃ showed a slightly larger Tafel slope than Pt/C (Figure 3h), similar to the case in acidic media; at large overpotentials, the Tafel slope of Ru/*a*-Ni-MoO₃ became much smaller than that of Pt/C (Figure S22, Supporting Information), which was reminiscent of the trend in alkaline media. In addition, Ru/*a*-Ni-MoO₃ showed comparable stability to Ru/C in the stability test, which was slightly inferior to that of Pt/C (Figure 3i, Table S4, Supporting Information). The EIS spectra and equivalent circuit fitting showed that the *R*_{ct} of Ru/*a*-Ni-MoO₃ (1.97 Ω) was lower than that of Ru/C (2.5 Ω), proving faster charge transfer (Figure S23, Table S5, Supporting Information).

Overall, these results suggested that Ru/*a*-Ni-MoO₃ was a pH-universal HER catalyst superior to Ru/C and comparable to Pt/C. In addition, the H₂ production rate of Ru/*a*-Ni-MoO₃ was measured in different pH media using gas chromatography (GC). As shown in Figure S24, Supporting Information, the experimentally measured H₂ amounts matched well with the theoretical values, resulting in Faraday efficiencies consistently over 90% and demonstrating the high H₂ production efficiency of Ru/*a*-Ni-MoO₃ (Table S6, Supporting Information). When comparing the performance of Ru/*a*-Ni-MoO₃ with other pH-universal HER catalysts reported in the recent literature,^[40–51] it possessed a unique advantage of showing both low η_{10} and small Tafel slopes in all three types of media (Figure 4a–c), confirming its high intrinsic activity and fast HER kinetics. In contrast, most catalysts only showed low values in one metric (either η_{10} or Tafel slope) in the three types of media or both metrics in just one type of medium. The combination of small η_{10} and Tafel slopes also can guarantee the low overpotentials to deliver large current densities which are desirable in practice. Indeed, Ru/*a*-Ni-MoO₃ exhibited superior and well-balanced

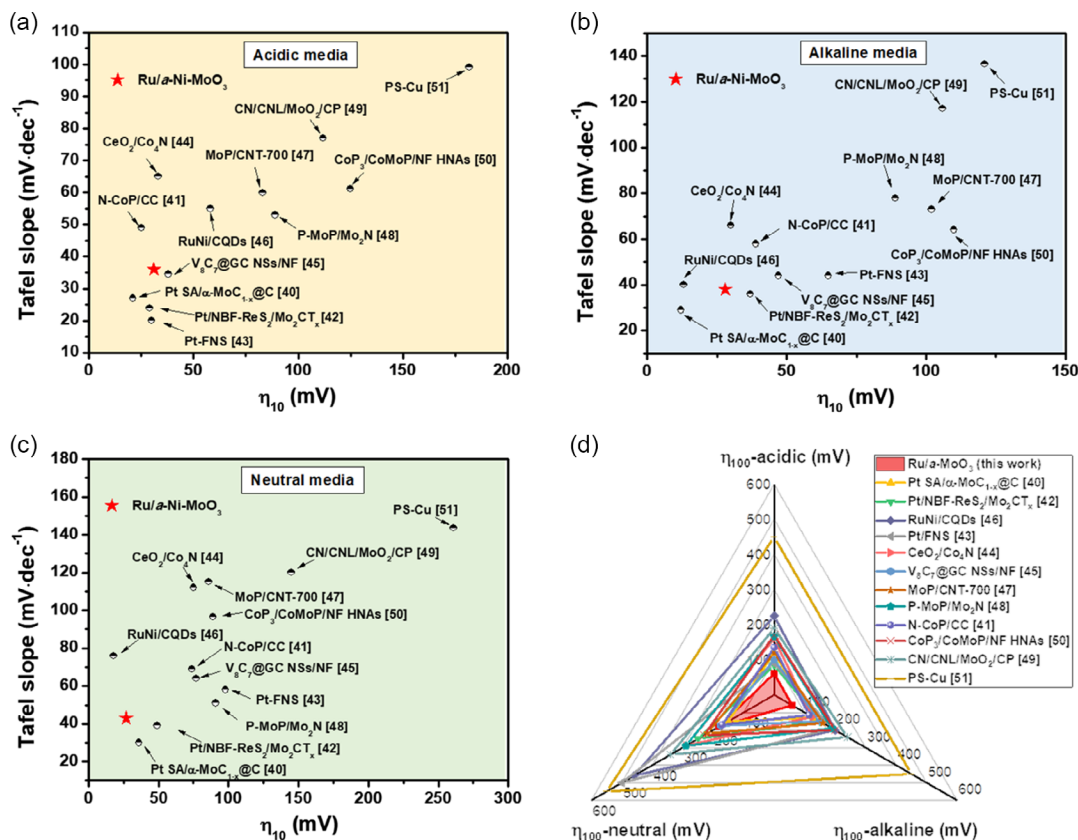


Figure 4. Comparison of η_{10} and Tafel slope of Ru/a-Ni-MoO₃ and other reported pH-universal HER catalysts in a) acidic, b) alkaline, and c) neutral media. d) Comparison of the large current density performance (η_{100}) of Ru/a-Ni-MoO₃ and other reported pH-universal HER catalysts.

HER performance at a high current density of 100 mA cm⁻² (Figure 4d), suggesting its potential for practical application. These comparisons therefore confirmed that Ru/a-Ni-MoO₃ could be an ideal candidate for pH-universal HER.

2.3. Catalytic Reaction Mechanism

To investigate the catalytic reaction mechanism, it is important to first determine the active sites in Ru/a-Ni-MoO₃. Considering that Ni was present in Ru/a-Ni-MoO₃, acid washing was conducted to confirm that it was not in the form of metallic Ni nanoparticles which are HER active. It was performed by immersing the electrode in 0.5 M H₂SO₄ for 22 h, the same as the immersion time to obtain Ru/a-Ni-MoO₃. As shown in Figure S25, Supporting Information, the HER performance of NiMoO₄-R degraded significantly after acid washing, indicating that Ni nanoparticles were the major active sites.^[23] In contrast, the HER performance of Ru/a-Ni-MoO₃ was barely affected by acid washing, showing that the contribution from metallic Ni was negligible in Ru/a-Ni-MoO₃. In addition, a-Ni-MoO₃ was the acid washing product of NiMoO₄-R after the removal of unstable Ni species. It showed significantly inferior performance in all three media to that of Ru/a-Ni-MoO₃ (Figure S26, Supporting Information). The performance enhancement provided by Ru was several hundred millivolts in overpotential

at a current density of 100 mA cm⁻². These results thus collectively proved that Ru was the active site in Ru/a-Ni-MoO₃.

Next, to provide theoretical insights into how the modified electronic structure of Ru active sites impacted HER performance, DFT calculations for the reaction coordinates were conducted. We have used amorphous MoO₃ (a-MoO₃) as the support to simplify computational modeling, since the above spectroscopic results indicated that Mo and Ni dopants were similarly affected by Ru. The DFT models of Ru/a-Ni-MoO₃ were thus constructed with Ru clusters on the a-MoO₃ support, with the amorphousness introduced by averaging different possible adsorption sites in the periodic MoO₃ surface (Figure 5a). Metallic Ru nanoparticles and a-MoO₃ were also used as comparisons in the modeling. Charge density difference analysis of Ru/a-MoO₃ showed that electrons were depleted at the Ru sites and accumulated in the a-MoO₃ support (Figure 5b). Moreover, the calculated electron density of Ru 4d states near the Fermi level in Ru/a-MoO₃ was noticeably lower than that in Ru (Figure 5c). These results agreed well with our experimental findings and verified the electronic structure modulation. The calculated energy diagram in Figure 5d showed that ΔG_{H^+} on the Ru sites of Ru/a-MoO₃ was -0.05 eV, a value that was close to 0 and favored for HER. The H⁺ desorption step was also facile because of the reduced energy barrier. In contrast, metallic Ru had a negative ΔG_{H^+} (-0.365 eV), suggesting its strong binding to H⁺, which was unfavorable in HER as it could impede the H⁺

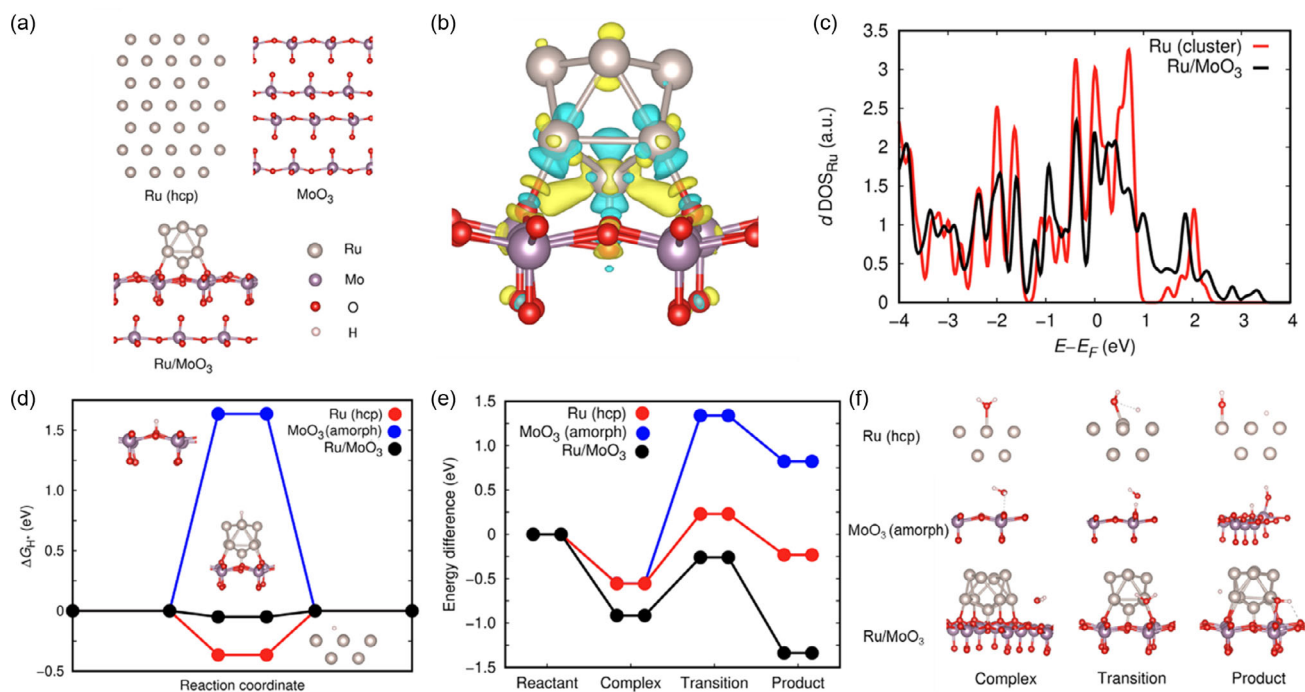


Figure 5. First-principles calculations based on DFT. a) Ball-stick models of Ru, *a*-MoO₃, and Ru/*a*-MoO₃. b) Charge density difference analysis of Ru/*a*-MoO₃; yellow and blue color indicate electronic accumulation and depletion respectively. c) Density of electronic d states of Ru and Ru/*a*-MoO₃. d) H* adsorption Gibbs free energies and the corresponding equilibrium geometries of Ru, *a*-MoO₃, and Ru/*a*-MoO₃. e) Transition paths and corresponding energy differences of H₂O molecular dissociation for Ru, *a*-MoO₃, and Ru/*a*-MoO₃. f) The most relevant configurations in H₂O molecular dissociation for Ru, *a*-MoO₃, and Ru/*a*-MoO₃.

desorption, while *a*-MoO₃ showed a large positive ΔG_{H^*} (1.636 eV), indicating its ineffective binding to H*. The DFT calculations therefore provided the link between the modulated electronic structure of Ru active sites and the enhanced HER performance, that is, the decreased density of states (DOS) of Ru near the Fermi level led to weakened interaction with H* and reduced energy barrier for the H* desorption step, resulting in accelerated HER kinetics.^[52]

In nonacidic media, slow HER kinetics is often associated with the sluggish water dissociation.^[11] As a result, even the benchmark Pt catalyst exhibits several orders of magnitude lower activity in nonacidic media than that in acidic solution.^[37] Considering this, the energy diagram of water dissociation process was also calculated to further elucidate the underlying HER mechanism in these media (Figure 5e), with the most relevant configurations illustrated in Figure 5f. The water dissociation energy barrier (ΔG_{H_2O}) for Ru was 0.79 eV, significantly lower than that of *a*-MoO₃ (1.89 eV). This finding indicated that Ru had a decent water dissociation capability, while *a*-MoO₃ was not so efficient. In Ru/*a*-MoO₃, the ΔG_{H_2O} on the Ru sites was further reduced to 0.66 eV, showing that the kinetic barrier of water dissociation was minimal. Moreover, water dissociation was only energetically favorable in Ru/*a*-MoO₃ among the three systems, as the energy of the “product” state (i.e., dissociated H₂O molecules) was 0.4 eV lower than that of the “complex” state (i.e., H₂O absorbed on the system). These results demonstrated that the water dissociation step was also effectively tuned by the modified electronic structure. It should be noted that the ΔG_{H_2O}

on Ru/*a*-MoO₃ was also much smaller than the value reported for Pt (0.94 eV) in the literature.^[37] The combination of both small ΔG_{H_2O} and ΔG_{H^*} thus contributed to a fast HER kinetics on Ru/*a*-Ni-MoO₃, accounting for its superior activity to Pt/C in nonacidic media (Figure 3d,g). Collectively, our theoretical investigation evidenced that the modulated electronic structure in the Ru/*a*-Ni-MoO₃ catalyst could facilitate both thermodynamics and kinetics of the HER steps, contributing to enhanced pH-universal HER performance.

3. Conclusion

In summary, we presented Ru/*a*-Ni-MoO₃ as a HER catalyst with superior performance in pH-universal media. The selection of Ru as the active material, with its high stability in acidic media and water dissociation capability in nonacidic media, laid the foundation for application in pH-universal environments. Based on this, further performance optimization was achieved in Ru/*a*-Ni-MoO₃ via electronic structure modulation. Through a combination of physicochemical characterizations, the structure of Ru/*a*-Ni-MoO₃ was found to be metallic Ru nanoparticles on the *a*-Ni-MoO₃ substrate. The electron transfer from Ru to *a*-Ni-MoO₃ effectively modulated the electronic structure of Ru active sites and resulted in a decreased DOS near the Fermi level. DFT calculations further demonstrated that the modulated electronic structure led to weakened interactions between the Ru active sites with H* and thus accelerated the

H* desorption process in all pH media. For nonacidic media, importantly, the sluggish water dissociation step was also facilitated by the optimized electronic structure. Our work thus shed light on the fabrication of pH-universal HER catalysts through a rational selection of materials and electronic structure modifications.

4. Experimental Section

Materials: Nickel (II) nitrate hexahydrate (Ni(NO₃)₂·6H₂O), sodium molybdate dihydrate (Na₂MoO₄·2H₂O), ruthenium chloride hydrate (RuCl₃·xH₂O), sodium phosphate monobasic hydrate (NaH₂PO₄·2H₂O), sodium phosphate dibasic (Na₂HPO₄), potassium hydroxide (KOH), 20 wt% Pt/C, and Nafion 117 solution were purchased from Sigma Aldrich. Sulfuric acid (H₂SO₄), nitric acid (HNO₃), and potassium permanganate (KMnO₄) were purchased from Chem-Supply. Carbon cloth and 20 wt% Ru/C were purchased from Fuel Cell Store. All chemicals were used as received.

Activation of Carbon Cloth (ACC): A piece of CC (4 × 4 cm²) was sequentially cleaned under sonication in 10% HNO₃ and deionized water (DI water) for 5 min each. Then, the cleaned CC was soaked in 5% KMnO₄ for 30 min before being taken out and rinsed with copious DI water. The ACC was then stored in DI water for further use.

Fabrication of NiMoO₄ Nanowires on ACC: 2 mmol Ni(NO₃)₂·6H₂O and 2 mmol Na₂MoO₄·2H₂O dissolved in 50 mL DI water were added into a 100 mL autoclave. A piece of ACC (4 × 4 cm²) was then transferred into the autoclave. The sealed autoclave was placed in electric oven under 150 °C for 6 h. After cooling down to room temperature, the electrode was taken out, rinsed with copious DI water, and dried overnight in an electric oven under 70 °C. After drying, NiMoO₄ on ACC was obtained.

Fabrication of NiMoO₄-R: NiMoO₄ on ACC was cut into pieces of 1 × 4 cm² and placed in a ceramic crucible. The crucible was then annealed in a tube furnace purged with 10% H₂/Ar at a flow rate of 100 mL min⁻¹. The annealing temperature was ramped to 400 °C at a rate of 2 °C min⁻¹ and kept for 2 h. After cooling down to room temperature, NiMoO₄-R on ACC was obtained.

Fabrication of Ru/a-Ni-MoO₃: NiMoO₄-R on ACC was immersed in 10 mL fresh 1 mg mL⁻¹ RuCl₃ solution for up to 22 h. After drying, the obtained electrode was Ru/a-Ni-MoO₃ on ACC.

Fabrication of Ru/C and Pt/C on ACC: The Ru/C or Pt/C catalyst ink was made by mixing 5 mg Ru/C or Pt/C catalyst, 1 mL ethanol, and 25 μL Nafion 117 solution and sonicating for 15 min. Then, 346 μL catalyst ink was transferred using a pipette and drop cast on ACC and dried before the test to give a similar noble metal loading (0.35 mg cm⁻²) to that in Ru/a-Ni-MoO₃.

Electrochemical Measurement: All electrochemical measurements were carried out by a CHI 750E electrochemical working station with a three-electrode cell purged with N₂ unless otherwise noted. HgO/Hg electrode was used as the reference electrode in alkaline media, while an SCE was used as the reference electrode in acidic and neutral media. A graphite rod was used as the counter electrode in all media. For measurement of H₂ amount, a gas-proof H-cell purged with Ar was used with a two-electrode setup where the working electrode and counter electrode were in separate compartments. Before test, the electrode was wrapped with Teflon tape to make sure the exposed area was 1 cm². All the reported polarization curves were conducted at a scan rate of 5 mV s⁻¹, which was manually corrected with 100% level *i*-R compensation. All the potentials reported were converted to reversed hydrogen electrode (RHE) unless otherwise noted. The conversion was performed based on the Nernst equation.^[53] The formula is given by $E_{vs. RHE} = E_{vs. Ref} + E_{Ref} + 0.0592 \cdot \text{pH}$, where $E_{vs. RHE}$ is the converted potential versus RHE, $E_{vs. Ref}$ is the experimentally applied potential versus the reference electrode, and E_{Ref} is the potential of the reference electrode against RHE. The E_{Ref} of the HgO/Hg used in alkaline media was 0.113 V, while that of the SCE electrode used in acidic and neutral media was 0.238 V. The pH of the electrolyte was measured by a pH meter. EIS was conducted from 10 K to 0.1 Hz with 5 mV amplitude.

Measurements of ECSA were conducted by cyclic voltammetry in non-Faradaic regions at scan rates of 40, 50, 60, 70, and 80 mV s⁻¹.^[54] The mean value of the absolute current density value at the middle point of positive and negative scans in the CV curves ($\Delta j/2$) was plotted against the scan rate. From the plot, the double-layer capacitance (C_{dl}) could be obtained with linear fitting based on the equation: $\Delta j/2 = \nu \cdot C_{dl}$, where ν is the scan rate. ECSA could then be calculated using the equation: $\text{ECSA} = C_{dl}/C_s$, where C_s is the general specific capacitance depending on the electrolyte. A C_s of 0.035 mF cm⁻² was used for acidic media, while 0.04 mF cm⁻² was used for neutral and alkaline media. The ESCA-normalized current density could be next obtained by dividing the experimentally measured current by ECSA. The measurement of H₂ production amount was performed by analyzing the gas product using GC after applying a cathodic current density of 20 mA cm⁻² for different time. The Faraday efficiency of H₂ production (η_{H_2}) was calculated based on the equation: $\eta_{H_2} = n_{H_2} / \frac{it}{96500 \cdot 2}$, where n_{H_2} is the measured amount of H₂, i is the current, t is the electrolysis time, 96 500 C mol⁻¹ is the Faraday constant, and 2 is the number of electrons required to generate one H₂ molecule.

Material Characterizations: SEM was performed using a FEI Nova NanoSEM 450 microscope. TEM and STEM-EDS were carried out with a JEOL JEM-F200 microscope. XRD was performed using a PANalytical Xpert Multipurpose XRD system with a Cu K α source ($\lambda = 1.54056 \text{ \AA}$). Raman spectroscopy was obtained using a Renishaw inVia Qontor Raman microscope with 514 nm diode laser. XPS and UPS were conducted on a Thermo ESCALAB250i X-ray photoelectron spectrometer using Al K α radiation. ICP-OES was carried out with a PerkinElmer Optima 7000 instrument. ICP-MS was carried out with a PerkinElmer Nexion 5000 instrument. GC measurement was performed with a Shimadzu GC-2010 instrument.

First-Principles Calculations: DFT calculations were performed to theoretically characterize the electronic and HER catalytic properties of hcp Ru nanoparticle, *a*-MoO₃ (amorphousness was considered by averaging over different possible adsorption sites on the regular MoO₃ surface), and hcp Ru nanoparticle on *a*-MoO₃.^[55] The PBEsol exchange-correlation energy functional was used as is implemented in the Vienna ab initio simulation package (VASP) software.^[56,57] The project-augmented wave (PAW) method was employed to represent the ionic cores by considering the following electrons as valence: Mo 4*p*, 5*s* and 4*d*; Ru 4*p*, 5*s* and 4*d*; O 2*s* and 2*p*; and H 1*s*.^[58] Wave functions were presented in a plane-wave basis truncated at 650 eV. For integrations within the first Brillouin zone, Monkhorst-Pack *k*-point grids were employed with a density equivalent to that of a 16 × 16 × 10 grid for the hcp bulk Ru unit cell. Periodic boundary conditions were applied along the three lattice vectors defining the simulation supercells. Geometry relaxations were performed with a conjugate-gradient algorithm that optimized the ionic positions, volume, and shape of the simulation cell. The relaxations were halted when the forces on the atoms were all below 0.005 eV \AA^{-1} . Using these technical parameters, total energies were converged to within 0.5 meV per formula unit.

For the H* and H₂O surface adsorption DFT calculations, large simulation cells were used containing about 2 nm-thick material slabs and 2.5 nm-thick vacuum regions (typically including around 200 atoms). The H* adsorption Gibbs free energy, ΔG_{H^*} , was calculated for the three analyzed systems using the standard thermochemical formula^[59,60]

$$\Delta G_{H^*} = \Delta E_{H^*} + \Delta E_{ZPE} + T\Delta S \quad (1)$$

where ΔE_{H^*} is the H* binding energy directly obtained from zero-temperature DFT calculations; ΔZPE is the zero-point energy difference between the molecule adsorbed on the oxide surface and in the gas phase; T is the temperature; and ΔS is the entropy difference. The temperature was fixed to 300 K in all thermochemical calculations and the VASPKIT code was used for postprocessing the data calculated with VASP.^[61]

Ab initio nudged elastic band (NEB) calculations were performed to estimate the energy barriers involved in the H₂O molecular dissociation for the three analyzed systems.^[61] The simulation supercell sizes and other technical parameters were the same as those employed in the above ΔG_{H^*}

calculations. The geometry optimizations were halted when the forces on the atoms were all smaller than 0.01 eV \AA^{-1} .

Supporting Information

Supporting Information is available from the Wiley Online Library or from the author.

Acknowledgements

All material and surface characterizations were carried out at the Mark Wainright Analytical Center (MWAC). This work was supported by an Australian Government Research Training Program (RTP) Scholarship and ARC Training Center for the Global Hydrogen Economy (IC200100023). Z.H. acknowledges Future Fellowship (FT220100209) from Australian Research Council. D.Z. acknowledges the UNSW UIPA PhD Scholarship.

Open access publishing facilitated by University of New South Wales, as part of the Wiley - University of New South Wales agreement via the Council of Australian University Librarians.

Conflict of Interest

The authors declare no conflict of interest.

Data Availability Statement

The data that support the findings of this study are available from the corresponding author upon reasonable request.

Keywords

electron transfers, electronic structures, hydrogen evolution reaction, pH universal, ruthenium

Received: June 3, 2023

Revised: July 17, 2023

Published online:

- [1] A. J. Ryan, R. H. Rothman, *Nat. Rev. Chem.* **2022**, *6*, 1.
- [2] Y. Zhao, P. V. Kumar, X. Tan, X. Lu, X. Zhu, J. Jiang, J. Pan, S. Xi, H. Y. Yang, Z. Ma, T. Wan, D. Chu, W. Jiang, S. C. Smith, R. Amal, Z. Han, X. Lu, *Nat. Commun.* **2022**, *13*, 2430.
- [3] Q. Zhang, Z. L. Zhe Ru, R. Daiyan, P. Kumar, J. Pan, X. Lu, R. Amal, *ACS Appl. Mater. Interfaces* **2021**, *13*, 53798.
- [4] W. Tong, M. Forster, F. Dionigi, S. Dresp, R. Sadeghi Erami, P. Strasser, A. J. Cowan, P. Farràs, *Nat. Energy* **2020**, *5*, 367.
- [5] M. Liu, H. Chen, X. Tang, H. Liu, B. Tu, W. Guo, Y. Zheng, Y. Liu, Y. Tang, R. He, W. Zhu, *Small* **2022**, *18*, 2107444.
- [6] J. Wei, M. Cao, K. Xiao, X. Guo, S. Ye, Z. Liu, *Small Struct.* **2021**, *2*, 2100047.
- [7] X. Wu, J. Qiu, Z. Wang, *Small Struct.* **2023**, *4*, 2200268.
- [8] Y. Liu, L. Gong, Y. Zhang, P. Wang, G. Wang, F. Bai, Z. Zhao, F. Gong, J. Liu, *Small Struct.* **2023**, *4*, 2200247.
- [9] Y. Wu, Y. Yi, Z. Sun, H. Sun, T. Guo, M. Zhang, L. Cui, K. Jiang, Y. Peng, J. Sun, *Chem. Eng. J.* **2020**, *390*, 124515.
- [10] I. Katsounaros, J. C. Meier, S. O. Klemm, A. A. Topalov, P. U. Biedermann, M. Auinger, K. J. J. Mayrhofer, *Electrochem. Commun.* **2011**, *13*, 634.
- [11] N. Danilovic, R. Subbaraman, D. Strmcnik, K. C. Chang, A. P. Paulikas, V. R. Stamenkovic, N. M. Markovic, *Angew. Chem. Int. Ed.* **2012**, *51*, 12495.
- [12] M. Ledendecker, J. S. Mondschein, O. Kasian, S. Geiger, D. Göhl, M. Schalenbach, A. Zeradjanin, S. Cherevko, R. E. Schaak, K. Mayrhofer, *Angew. Chem. Int. Ed.* **2017**, *56*, 9767.
- [13] M. C. Weidman, D. V. Esposito, I. J. Hsu, J. G. Chen, *J. Electrochem. Soc.* **2010**, *157*, F179.
- [14] Y. Zhang, L. Gao, E. J. M. Hensen, J. P. Hofmann, *ACS Energy Lett.* **2018**, *3*, 1360.
- [15] Q. Ma, C. Hu, K. Liu, S. F. Hung, D. Ou, H. M. Chen, G. Fu, N. Zheng, *Nano Energy* **2017**, *41*, 148.
- [16] M. Pourbaix, *Atlas of Electrochemical Equilibria in Aqueous Solution*, Pergamon Press **1966**, p. 346.
- [17] S. Zhu, X. Qin, F. Xiao, S. Yang, Y. Xu, Z. Tan, J. Li, J. Yan, Q. Chen, M. Chen, M. Shao, *Nat. Catal.* **2021**, *4*, 711.
- [18] C. Li, H. Jang, M. G. Kim, L. Hou, X. Liu, J. Cho, *Appl. Catal., B* **2022**, *307*, 121204.
- [19] J. K. Nørskov, T. Bligaard, A. Logadottir, J. R. Kitchin, J. G. Chen, S. Pandelov, U. Stimming, *J. Electrochem. Soc.* **2005**, *152*, j23.
- [20] X. Kong, K. Xu, C. Zhang, J. Dai, S. Norooz Olliaee, L. Li, X. Zeng, C. Wu, Z. Peng, *ACS Catal.* **2016**, *6*, 1487.
- [21] X. Xiao, X. Wang, X. Jiang, S. Song, D. Huang, L. Yu, Y. Zhang, S. Chen, M. Wang, Y. Shen, Z. Ren, *Small Methods* **2020**, *4*, 1900796.
- [22] D. Guo, Y. Luo, X. Yu, Q. Li, T. Wang, *Nano Energy* **2014**, *8*, 174.
- [23] L. Peng, J. Min, A. Bendavid, D. Chu, X. Lu, R. Amal, Z. Han, *ACS Appl. Mater. Interfaces* **2022**, *14*, 40822.
- [24] Y. Ding, Z. Shi, Y. Sun, J. Wu, X. Pan, J. Sun, *ACS Nano* **2023**, *17*, 6002.
- [25] Y. Wang, X. Xu, Z. Tian, Y. Zong, H. Cheng, C. Lin, *Chem. Eur. J.* **2006**, *12*, 2542.
- [26] K. Ajito, L. A. Nagahara, D. A. Tryk, K. Hashimoto, A. Fujishima, *J. Phys. Chem.* **1995**, *99*, 16383.
- [27] N. Bala, H. K. Singh, S. Verma, S. Rath, *Phys. Rev. B* **2020**, *102*, 024423.
- [28] Y. Zhou, Z. Xie, J. Jiang, J. Wang, X. Song, Q. He, W. Ding, Z. Wei, *Nat. Catal.* **2020**, *3*, 454.
- [29] H. Yang, Z. Chen, P. Guo, B. Fei, R. Wu, *Appl. Catal., B* **2020**, *261*, 118240.
- [30] D. J. Morgan, *Surf. Interface Anal.* **2015**, *47*, 1072.
- [31] L. Li, C. Liu, S. Liu, J. Wang, J. Han, T. Chan, Y. Li, *ACS Nano* **2022**, *16*, 14885.
- [32] J. Baltrusaitis, B. Mendoza-Sanchez, V. Fernandez, R. Veenstra, N. Dukstiene, A. Roberts, N. Fairley, *Appl. Surf. Sci.* **2015**, *326*, 151.
- [33] M. C. Biesinger, B. P. Payne, L. W. M. Lau, A. Gerson, R. S. C. Smart, *Surf. Interface Anal.* **2009**, *41*, 324.
- [34] A. Bruix, J. A. Rodriguez, P. J. Ramirez, S. D. Senanayake, J. Evans, J. B. Park, D. Stacchiola, P. Liu, J. Hrbek, F. Illas, *J. Am. Chem. Soc.* **2012**, *134*, 8968.
- [35] B. E. Conway, B. V. Tilak, *Electrochim. Acta* **2002**, *47*, 3571.
- [36] A. R. J. Kucernak, V. N. Naranammalpuram Sundaram, *J. Mater. Chem. A* **2014**, *2*, 17435.
- [37] Y. Zheng, Y. Jiao, Y. Zhu, L. H. Li, Y. Han, Y. Chen, M. Jaroniec, S. Z. Qiao, *J. Am. Chem. Soc.* **2016**, *138*, 16174.
- [38] C. Costentin, D. G. Nocera, *Proc. Natl. Acad. Sci. U. S. A.* **2017**, *114*, 13380.
- [39] Z. Zhou, Z. Pei, L. Wei, S. Zhao, X. Jian, Y. Chen, *Energy Environ. Sci.* **2020**, *13*, 3185.
- [40] W. Wang, Y. Wu, Y. Lin, J. Yao, X. Wu, C. Wu, X. Zuo, Q. Yang, B. Ge, L. Yang, G. Li, S. Chou, W. Li, Y. Jiang, *Adv. Funct. Mater.* **2021**, *32*, 2108464.
- [41] Y. Men, P. Li, F. Yang, G. Cheng, S. Chen, W. Luo, *Appl. Catal., B* **2019**, *253*, 21.

- [42] M. Yi, N. Li, B. Lu, L. Li, Z. Zhu, J. Zhang, *Energy Storage Mater.* **2021**, 42, 418.
- [43] C. Zhang, Y. Cui, Y. Yang, L. Lu, S. Yu, Z. Meng, Y. Wu, Y. Li, Y. Wang, H. Tian, W. Zheng, *Adv. Funct. Mater.* **2021**, 31, 2105372.
- [44] N. Yao, R. Meng, F. Wu, Z. Fan, G. Cheng, W. Luo, *Appl. Catal., B* **2020**, 277, 119282.
- [45] H. Xu, J. Wan, H. Zhang, L. Fang, L. Liu, Z. Huang, J. Li, X. Gu, Y. Wang, *Adv. Energy Mater.* **2018**, 8, 1800575.
- [46] Y. Liu, X. Li, Q. Zhang, W. Li, Y. Xie, H. Liu, L. Shang, Z. Liu, Z. Chen, L. Gu, Z. Tang, T. Zhang, S. Lu, *Angew. Chem. Int. Ed.* **2020**, 59, 1718.
- [47] X. Zhang, X. Yu, L. Zhang, F. Zhou, Y. Liang, R. Wang, *Adv. Funct. Mater.* **2018**, 28, 1706523.
- [48] H. Fu, Y. Gu, A. Wu, Y. Jiao, H. Zheng, X. Wang, Y. Xie, L. Wang, C. Tian, *Angew. Chem. Int. Ed.* **2021**, 60, 6673.
- [49] J. Dong, X. Zhang, J. Huang, J. Hu, Z. Chen, Y. Lai, *Chem. Eng. J.* **2021**, 412, 128556.
- [50] D. Jiang, Y. Xu, R. Yang, D. Li, S. Meng, M. Chen, *ACS Sustainable Chem. Eng.* **2019**, 7, 9309.
- [51] W. J. Kang, Y. Feng, Z. Li, W. Q. Yang, C. Q. Cheng, Z. Z. Shi, P. F. Yin, G. R. Shen, J. Yang, C. K. Dong, H. Liu, F. X. Ye, X. W. Du, *Adv. Funct. Mater.* **2022**, 32, 2112367.
- [52] C. Tsounis, B. Subhash, P. V. Kumar, N. M. Bedford, Y. Zhao, J. Shenoy, Z. Ma, D. Zhang, C. Y. Toe, S. Cheong, R. D. Tilley, X. Lu, L. Dai, Z. Han, R. Amal, *Adv. Funct. Mater.* **2022**, 32, 2203067.
- [53] K. Kawashima, R. A. Márquez, Y. J. Son, C. Guo, R. R. Vaidyula, L. A. Smith, C. E. Chukwunneke, C. B. Mullins, *ACS Catal.* **2023**, 13, 1893.
- [54] C. C. L. McCrory, S. Jung, I. M. Ferrer, S. M. Chatman, J. C. Peters, T. F. Jaramillo, *J. Am. Chem. Soc.* **2015**, 137, 4347.
- [55] C. Cazorla, J. Boronat, *Rev. Mod. Phys.* **2017**, 89, 035003.
- [56] J. P. Perdew, A. Ruzsinszky, G. I. Csonka, O. A. Vydrov, G. E. Scuseria, L. A. Constantin, X. Zhou, K. Burke, *Phys. Rev. Lett.* **2008**, 100, 136406.
- [57] G. Kresse, J. Furthmüller, *Phys. Rev. B* **1996**, 54, 11169.
- [58] P. E. Blöchl, *Phys. Rev. B* **1994**, 50, 17953.
- [59] S. Siahrostami, A. Verdager-Casadevall, M. Karamad, D. Deiana, P. Malacrida, B. Wickman, M. Escudero-Escribano, E. A. Paoli, R. Frydendal, T. W. Hansen, I. Chorkendorff, I. E. L. Stephens, J. Rossmeisl, *Nat. Mater.* **2013**, 12, 1137.
- [60] Z. Liu, B. Wang, C. Cazorla, *ACS Sustainable Chem. Eng.* **2022**, 10, 16924.
- [61] V. Wang, N. Xu, J. C. Liu, G. Tang, W. T. Geng, *Comput. Phys. Commun.* **2021**, 267, 108033.